A Petrov-Galerkin Natural Element Method Securing the Numerical Integration Accuracy

Jin-Rae Cho*, Hong-Woo Lee
School of Mechanical Engineering, Pusan National University, Kumjung-Ku, Busan 609-735, Korea

An improved meshfree method called the Petrov-Galerkin natural element (PG-NE) method is introduced in order to secure the numerical integration accuracy. As in the Bubnov-Galerkin natural element (BG-NE) method, we use Laplace interpolation function for the trial basis function and Delaunay triangles to define a regular integration background mesh. But, unlike the BG-NE method, the test basis function is differently chosen, based on the Petrov-Galerkin concept, such that its support coincides exactly with a regular integration region in background mesh. Illustrative numerical experiments verify that the present method successfully prevents the numerical accuracy deterioration stemming from the numerical integration error.

Key Words: Petrov-Galerkin Natural Element Method, Laplace Interpolation Function, Constant Strain Basis Function, Numerical Integration Accuracy, Convergence Assessment

1. Introduction

For several decades, finite element method has been widely and successfully used to obtain approximate solutions of mathematical problems encountered in most engineering and applied science fields. The subdivision of a problem domain into a finite number of elements, called finite element mesh, provides a systematic way to define basis functions, even for the extremely complex domains. However, the use of finite element mesh does also possess several inherent drawbacks, at the same time, such as the requirement of the element connectivity preservation, the numerical quality deterioration or simulation incompleteness owing to the excessive mesh distortion (Cho and Lee, 2002), and the painstaking mesh adaptation process.

* Corresponding Author,
E-mail : jrcho@pusan.ac.kr
TEL : +82-51-510-2467; **FAX** : +82-51-514-7640
School of Mechanical Engineering, Pusan National University, Kumjung-Ku, Busan 609-735, Korea.
(Manuscript **Received** June 17, 2005; **Revised** December 12, 2005)

In connection with these demerits of FEM, many investigators have focused on the concept of meshfree (meshless) method since Nayroles et al.(1992) presented the diffuse element method (DEM). As a result, this concept has been settled down within a relatively short period of time, so that its application to major engineering problems has been accomplished to some extent. Among the meshfree methods introduced so far are the element free Galerkin method (EFGM) by Belytschko et al.(1994), the reproducing kernel particle method (RKPM) by Liu et al.(1995), the h-p clouds by Duarte and Oden (1996), the partition of unity method (PUM) by Melenk and Babuska (1996), and the meshless local Petrov-Galerkin (MLPG) method by Atluri et al.(1998).

However, these methods suffer from the common difficulties in the numerical implementation, the enforcement of essential boundary condition and the numerical integration. To resolve the former difficulty stemming from the violation of the Kronecker delta property of basis functions, the employment of alternative numerical techniques such as the penalty method (Zhu and Atluri, 1998) and the Lagrange multiplier

method (Belytschko et al., 1994) has been tried. The latter difficulty requires the generation of undesired background mesh so as to utilize the conventional regular Gauss quadrature rule. But, this kind of numerical integration causes the considerable integration accuracy deterioration (Dolbow and Belytschko, 1999). One is because the basis functions used in meshfree methods are not polynomial but rational, the other is because the support of integrand function does not coincide with a regular integration domain within background mesh. Here, the latter factor has been reported to be more crucial than the former.

Recently, the natural element method based on the natural neighbors (Braun and Sambridge, 1995) and the Bubnov-Galerkin approximation is being explored as a possible solution to the above-mentioned defects of meshfree methods (Sukumar et al., 1998). In which, Laplace (or non-Sibsonian) interpolation functions, which are defined by the Voronoi diagram and the Delaunay triangulation, are used for both trial and test basis functions. Thanks to the Kronecker delta property of Laplace interpolation functions, essential boundary condition can be strictly enforced for both convex and non-convex domains without any additional numerical technique (Cueto et al., 2002). As well as, those functions can be suitably constructed even for irregularly distributed nodes, because those are defined in terms of the geometry information of nodes. Nevertheless, the Bubnov-Galerkin natural element method possesses the numerical integration difficulty as ever, because the support of integrand function does not coincide with a regular integration region in background mesh.

In order to resolve the numerical integration problem of natural element method, we introduce an improved natural element method based on the Petrov-Galerkin approximation. While Laplace interpolation function is being taken for the trial basis function, the test basis function in the present method is differently defined such that its support becomes a union of Delaunay triangles. This approach eliminates the inconsistency of the support of integrand function with the regular integration domain, and which preserves both simplicity and accuracy in the numerical integration. The validity of the proposed method is verified through the representative benchmark experiments.

2. Voronoi Diagram and Delaunay Triangulation

We consider a two-dimensional Euclidean space $\Re^2$ for the sake of simple representation of the Voronoi diagram and the Delaunay triangulation. When a set $\aleph$ of N distinct points (or nodes) : $\aleph=\{\boldsymbol{x}_1, \boldsymbol{x}_2, \cdots, \boldsymbol{x}_N \mid \boldsymbol{x}_I \in \Re^2\}$ is assumed to be given, then its first-order Voronoi diagram V_I is defined by N Voronoi polygons ω_N such that $V_I=\{\omega_1, \omega_2, \cdots, \omega_N \mid \overline{\omega_1 \cup \cdots \cup \omega_N}=\Re^2\}$. In which, the Voronoi polygon ω_I corresponding to the I-th node is defined by

$$\omega_I=\{\boldsymbol{x}\in\Re^2 : d(\boldsymbol{x}, \boldsymbol{x}_I)<d(\boldsymbol{x}, \boldsymbol{x}_J),\ \forall J\neq I\} \quad (1)$$

with the Euclidean metric $d(\boldsymbol{x}, \boldsymbol{x}_I)$ in $\Re^2$ (Green and Sibson, 1978, Okabe et al., 1992).

Referring to Fig. 1(a), the I-th Voronoi polygon ω_I is a sub-domain with its sides that perpendicularly bisect the lines connecting $\boldsymbol{x}_I$ and adjacent neighbor nodes. Vertex points of each Voronoi polygon are called the Voronoi vertices, and the domain enclosed by the outer lines connecting nodes is defined as the convex hull $\Omega^{CH}(\aleph)$ of N points. When node is located on the boundary of the convex hull $\Omega^{CH}(\aleph)$, its Voronoi polygon becomes unbounded as shown in Fig. 1(a).

Referring to Fig. 1(b), the Delaunay triangulation as a geometric dual of the Voronoi diagram generates a set $\Im$ of Delaunay triangles $\Delta_{JKL}(\boldsymbol{x})$:

$$\Im=\{\Delta_{JKL}(\boldsymbol{x}) : \cup\overline{\Delta_{JKL}}=\Omega^{CH}(\aleph),\ J\neq K\neq L\} \quad (2)$$

where J, K and L refer to the nodes $\boldsymbol{x}_J$, $\boldsymbol{x}_K$ and $\boldsymbol{x}_L$ become three vertices of Δ_{JKL}. In general, the convex hull becomes the problem domain : $\Omega^{CH}(\aleph)\equiv\Omega$. Referring to Fig. 1(a), these three vertex nodes should be chosen such that three corresponding Voronoi polygons share common edges. The reader may refer to Okabe et al. (1992) for the discussion on the geometric dual

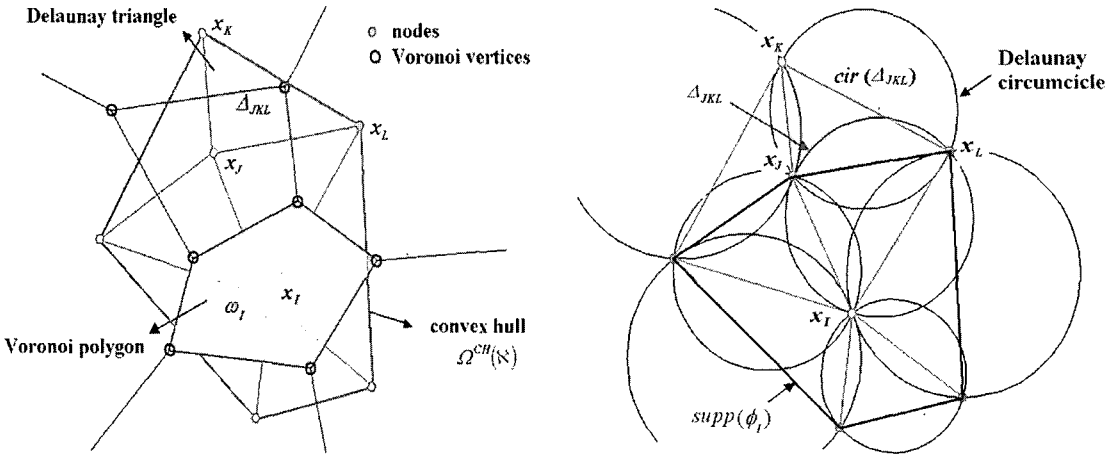

Fig. 1 Representation : (a) Voronoi diagram and Delaunay triangulation ; (b) Delaunay circumcircles

relation between $\Im$ and V_I. An important property of the Delaunay triangulation is the empty circumcircle criterion implying that individual Delaunay circumcircles should not contain any node in $\aleph$. Also, it is worth to note that the centers of these circumcircles identically become the Voronoi vertices.

Referring to Fig. 1(a), the Voronoi polygon ω_I shares its sides with five Voronoi polygons, and such neighborhood polygons are called the natural neighbors of ω_I. In the same manner, the five nodes within five natural neighbors of ω_I are defined as the natural neighbors of the node $\boldsymbol{x}_I$. These natural neighbors serve a basis for constructing Sibsonian interpolation functions. The concept of the natural neighbors and the Sibsonian interpolation was introduced by Sibson (1980) originally for curve fitting and smoothing.

3. Non-Sibsonian Interpolation and Laplace Interpolation Functions

As another interpolation method based on the natural neighbors, there exists the non-Sibsonian (or, called Laplace) interpolation introduced by Belikov et al.(1997) and Hiyoshi and Sugihara (1999), from which Laplace interpolation functions are derived. In both Sibsonian and non-Sibsonian interpolation, the second-order Voronoi diagram V_{II} is commonly introduced to define interpolation functions. Referring to Fig. 2(a), let us consider a point $\boldsymbol{x}_P$ in the first-order Voronoi diagram depicted in Fig. 1(a). Then, this point does also define a new first-order Voronoi polygon ω_P, and which is divided into four sub-regions by the previously defined Voronoi polygons ω_I. These sub-regions are called the second-order Voronoi cells ω_{PI} which are geometrically defined by

$$\omega_{PI}=\{\boldsymbol{x}\in\Re^2 : d(\boldsymbol{x}, \boldsymbol{x}_P)<d(\boldsymbol{x}, \boldsymbol{x}_I)<d(\boldsymbol{x}, \boldsymbol{x}_J), \quad \forall J\neq P, I\} \tag{3}$$

The second-order Voronoi diagram is defined based on the first-order Voronoi diagram V_I but the number of ω_{PI} is not identical with the number of nodes, so that the shapes of Voronoi polygon ω_P and corresponding second-order Voronoi cells vary with the choice of point $\boldsymbol{x}_P$.

In the Sibsonian interpolation method, interpolation functions are defined in terms of the relative area ratios of ω_{PI} to the total area of ω_P, as described in Sukumar et al.(1998). On the other hand, Laplace interpolation functions in the non-Sibsonian case are expressed in the slightly different manner. Referring to Fig. 2(b), we first introduce the weighting functions a_I defined by

$$a_I(\boldsymbol{x}_P)=\frac{s_I(\boldsymbol{x}_P)}{h_I(\boldsymbol{x}_P)},\quad I=1, 2, \cdots, M \tag{4}$$

where $h_I=d(\boldsymbol{x}_P, \boldsymbol{x}_I)/2$ and s_I denotes the length

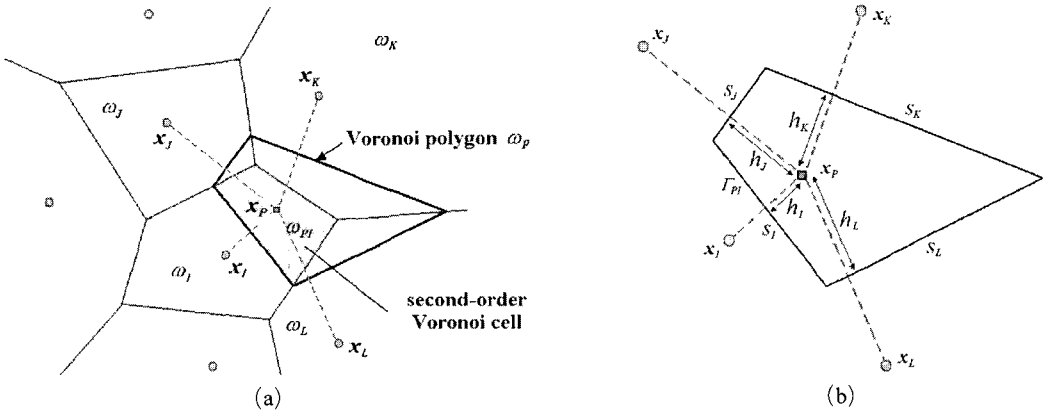

Fig. 2 Definition: (a) second-order Voronoi cells of x_P; (b) geometric definition of the polygon ω_P

of the side Γ_{PI}. Here, the subscript I designates the edge of ω_P facing to the node number x_I and M denotes the number of natural neighbors of the polygon ω_P. Then, the values of M Laplace interpolation functions at the point x_P are determined through

$$\phi_I(x_P)=\alpha_I(x_P)/\sum_{I=1}^{M}\alpha_I(x_P),\ I=1,\ 2,\ \cdots,\ M \quad (5)$$

In numerical implementation aspects, the computation of Laplace interpolation functions at the specific point (usually at Gaussian point) is more effective, when compared to Sibsonian interpolation functions, because it requires only the calculation of lengths.

In this manner, we can define all Laplace interpolation functions for a given set $\aleph$ of N nodes. It is worthy noting that the total number of functions coincides with the total node number. Since x_P is an arbitrary point in the Voronoi diagram V_I, we drop the subscript P in x_P hereafter. When we restrict to the I-th Laplace interpolation function $\phi_I(x)$, its support becomes the intersection of the convex hull $\Omega^{CH}(\aleph)$ shown in Fig. 1(b) with the Delaunay circumcircles defined by the node x_I and its neighbor nodes (Farin, 1990):

$$supp(\phi_I(x))=\cup\overline{cir(\Delta_{IJK}(x))}\cap\Omega^{CH}(\aleph) \quad (6)$$

The support of the Laplace interpolation function with respect to its node position within a uniform grid is illustrated in Fig. 3(a). Where, two nodes J and K have the supports bounded by the convex hull of nodes. Fig. 3(b) represents three Laplace interpolation functions ϕ_I, ϕ_J and ϕ_K plotted according to Eq. (5). Where, we see that ϕ_I becomes peak at node I and vanishes at

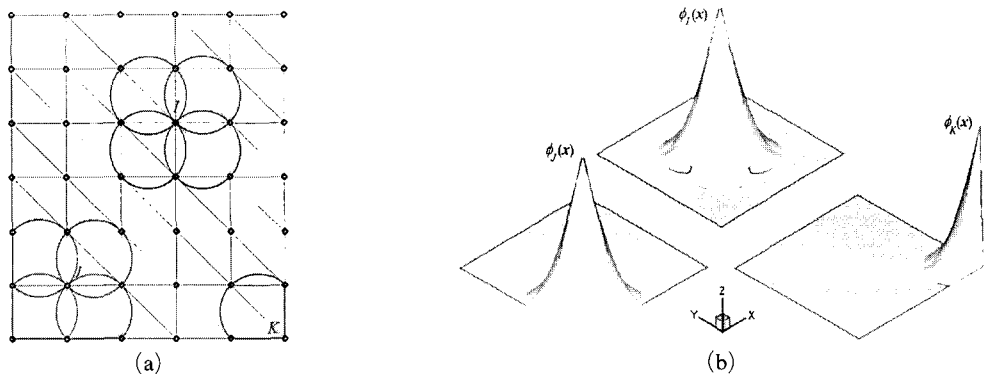

Fig. 3 Uniform grid: (a) function supports; (b) function shapes

the boundary of its support. On the other hand, ϕ_J does also vanish at the boundary region $supp(\phi_J) \cap \Gamma$ and ϕ_K shows a linear variation along the boundary. These features of Laplace interpolation functions will be described in details in Section 4.2.

Referring to Eq. (5), together with the plots of $\phi_I(x)$ shown in Fig. 3(b), Laplace interpolation functions possess the following basic properties:

$$0 \le \phi_I(x) \le 1 : \textit{positivity} \tag{7}$$

$$\phi_I(\boldsymbol{x}_J) = \delta_{IJ} : \textit{Kronecker delta} \tag{8}$$

$$\sum_{I=1}^{N} \phi_I(\boldsymbol{x}) = 1, \ \forall \boldsymbol{x} \in \Omega : \textit{partition of unity} \tag{9}$$

$$\boldsymbol{x} = \sum_{I=1}^{N} \phi_I(\boldsymbol{x}) \boldsymbol{x}_I : \textit{linear consistency} \tag{10}$$

Three properties (7)-(9) can be easily realized from the definition (5), while the last property (10) implies that any bilinear field can be exactly preserved by the Laplace interpolation (Piper, 1993). On the other hand, one can easily derive the spatial derivatives of $\phi_I(\boldsymbol{x})$ given by

$$\phi_{I,\beta}(\boldsymbol{x}) = \frac{\alpha_{I,\beta}(\boldsymbol{x}) - \phi_I(\boldsymbol{x}) \sum_{l=1}^{M} \alpha_{l,\beta}(\boldsymbol{x})}{\sum_{l=1}^{M} \alpha_l(\boldsymbol{x})}, \ \beta = x, y \tag{11}$$

with $\alpha_{I,\beta}(\boldsymbol{x}) = \lfloor s_{I,\beta}(\boldsymbol{x}) - \alpha_I h_{I,\beta}(\boldsymbol{x}) \rfloor / h_I(\boldsymbol{x})$. Here, spatial derivatives of h_I and s_I are obtained by differentiating the corresponding line equations that are defined with the geometric co-ordinates of two end points.

4. Petrov-Galerkin Natural Element (PG-NE) Method

We consider a two-dimensional linear elastic material occupying the domain $\Omega \in \Re^2$ for the current study. Then, its deformation field $\boldsymbol{u}$ is governed by

$$\sigma_{\alpha\beta}(\boldsymbol{u})_{,\beta} + b_\alpha = 0, \text{ in } \Omega \tag{12}$$

equipped with

$$u_\alpha = \hat{u}_\alpha, \text{ on } \Gamma_D \tag{13}$$

$$\sigma_{\alpha\beta} n_\beta = \hat{t}_\alpha, \text{ on } \Gamma_N \tag{14}$$

Here, $\boldsymbol{b}$ is the body force and $\boldsymbol{n}$ the outward unit vector normal to the boundary $\Gamma = \overline{\Gamma_D \cup \Gamma_N}$. And, the constitutive and compatibility relations are

$$\sigma_{\alpha\beta} = C_{\alpha\beta\gamma\delta} \varepsilon_{\gamma\delta} \tag{15}$$

$$\varepsilon_{\gamma\delta} = (u_{\gamma,\delta} + u_{\delta,\gamma})/2 \tag{16}$$

with the material constant tensor $\boldsymbol{C}$. The virtual work principle converts the boundary value problem (11) to the variational formulation: Find $\boldsymbol{u}$ such that

$$\int_\Omega \sigma_{\alpha\beta}(\boldsymbol{u}) \varepsilon_{\alpha\beta}(\boldsymbol{v}) \, d\Omega = \int_\Omega b_\alpha v_\alpha d\Omega + \int_{\Gamma_N} \hat{t}_\alpha v_\alpha ds \tag{17}$$

for every admissible virtual displacement $\boldsymbol{v}$.

In order for the natural element approximation, trial and test functions are expanded as

$$u_\alpha(\boldsymbol{x}) = \sum_{J=1}^{N} \bar{u}_\alpha^J \phi_J(\boldsymbol{x}) \tag{18}$$

$$v_\alpha(\boldsymbol{x}) = \sum_{I=1}^{N} \bar{v}_\alpha^I \psi_I(\boldsymbol{x}) \tag{19}$$

for a given natural element grid composed of N nodes (refer to Fig. 1(a)). Introducing Eqs. (18) and (19) into Eqs. (15)-(17) leads to

$$\sum_{I}^{N} \boldsymbol{K}^I \bar{\boldsymbol{u}} = \sum_{I}^{N} F^I \tag{20}$$

with the $(2N \times 1)$ nodal vector $\bar{\boldsymbol{u}}$ and the node-wise matrices defined by

$$\boldsymbol{K}^I = \int_{\Omega_v^I} (\boldsymbol{D}\Psi)^T \boldsymbol{C} (\boldsymbol{D}\Phi) \, d\Omega \tag{21}$$

$$\boldsymbol{F}^I = \int_{\Omega_v^I} \Psi^T \boldsymbol{b} d\Omega + \int_{\Gamma_N \cap \Omega_v^I} \Psi^T \hat{t} \, ds \tag{22}$$

in which $\Omega_v^I = supp(\psi_I(\boldsymbol{x}))$ and D is the (3×2) divergence-like operator defining Cauchy strain tensor. And, two matrices Ψ and Φ are

$$\Psi = \left[\begin{pmatrix} \psi_1 & 0 \\ 0 & \psi_1 \end{pmatrix} \cdots \begin{pmatrix} \psi_I & 0 \\ 0 & \psi_I \end{pmatrix} \cdots \begin{pmatrix} \psi_N & 0 \\ 0 & \psi_N \end{pmatrix} \right] \tag{23}$$

$$\Phi = \left[\begin{pmatrix} \phi_1 & \phi \\ 0 & 0_1 \end{pmatrix} \cdots \begin{pmatrix} \phi_J & 0 \\ 0 & \phi_J \end{pmatrix} \cdots \begin{pmatrix} \phi_N & 0 \\ 0 & \phi_N \end{pmatrix} \right] \tag{24}$$

Eq. (20) implies that the numerical integration in natural element methods is carried out over the support of each test basis function.

In the BG-NE method, Sibsonian or non-Sibsonian interpolation function is used commonly for both trial and test basis functions. But, for the current PG-NE method, while using Laplace interpolation function for trial basis function,

we use different functions supported on Delaunay triangles for test basis function. By using different basis functions in this manner, we intend to achieve both the numerical integration accuracy and the easy application of conventional Gauss quadrature rule.

4.1 Numerical integration in the PG-NE method

The numerical integration in most meshfree methods is usually performed by the Gauss quadrature rule devised for conventional finite element method, and for which the construction of background meshes is an indispensable requirement. Since a background mesh in the natural element method is automatically constructed with Delaunay triangles generated a priori in the definition process of basis functions, additional efforts for constructing background mesh are not required differing from the other meshfree methods. However, the BG-NE method still suffers from the numerical integration inaccuracy owing to the discrepancy between the support of test basis function and the integration domain of the regular triangular finite elements. As pointed in a book by Strang and Fix (1973), the numerical integration using the Gauss quadrature rule shows the deterioration in both numerical accuracy and convergence rate when the support of integrand function does not coincide with a regular integration region in background mesh.

Let us consider a uniform grid in order to examine the case of the BG-NE method. As shown in Figs. 3(a) and 4, neither the support of test basis function ψ_I nor the intersection Ω_{int}^{IJ} between ψ_I and ϕ_J does not coincide with a union of Delaunay triangles to which the regular Gauss quadrature rule is applied. As a result, one encounters the numerical difficulties in calculating $\boldsymbol{K}^I$ and $\boldsymbol{F}^I$ in Eqs. (21) and (22). In order to overcome this problem, Dolbow and Belytschko (1999) employed the bounding box technique to construct a background mesh in which the regular integration domain exactly coincides with the support of test basis function. However, not only such a background mesh is hard to construct owing to the geometric complexity of Ω_{int}^{IJ}, but also it is difficult for such a complicated background mesh to seek an appropriate quadrature rule. Meanwhile, Traversoni (1994) tried to transform the irregular integration regions composed of Delaunay circumcircles into regular ones. However, this approach requires a considerable complexity in deriving the mapping functions.

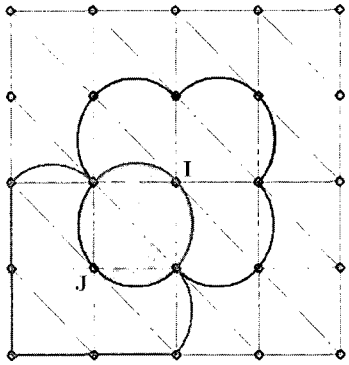

Fig. 4 Intersection region Ω_{int}^{IJ} between test and trial basis functions in the BG-NE method

On the other hand, the PG-NE method uses the constant strain finite element (CS-FE) basis function as the test basis function. Referring to Fig. 5(a), its support is composed of a union of Delaunay triangles, so that the discrepancy between the regular Gauss integration domain and the test function support does not occur any more. Thus, the integration of $\boldsymbol{F}^I$ in Eq. (22) can be accurately and easily performed as in conventional finite element method, without requiring any additional numerical technique. Furthermore, the intersection region Ω_{int}^{IJ} between the CS-FE basis function ψ_I and Laplace basis function ϕ_J is always contained within $supp(\psi_I)$. Thus, one can accurately and easily obtain $\boldsymbol{K}^I$ in Eq. (21) by applying the Gauss quadrature rule, as in the finite element method.

For reference, three shape functions $\hat{\psi}_i$ supported on individual Delaunay triangles are easily defined by

$$\hat{\psi}_1(x, y)=\{(x_2y_3-x_3y_2)+(y_2-y_3)x+(x_3-x_2)y\}/2A \quad (25)$$

$$\hat{\psi}_2(x, y)=\{(x_3y_1-x_1y_3)+(y_3-y_1)x+(x_1-x_3)y\}/2A \quad (26)$$

$$\hat{\psi}_3(x, y)=\{(x_1y_2-x_2y_1)+(y_1-y_2)x+(x_2-x_1)y\}/2A \quad (27)$$

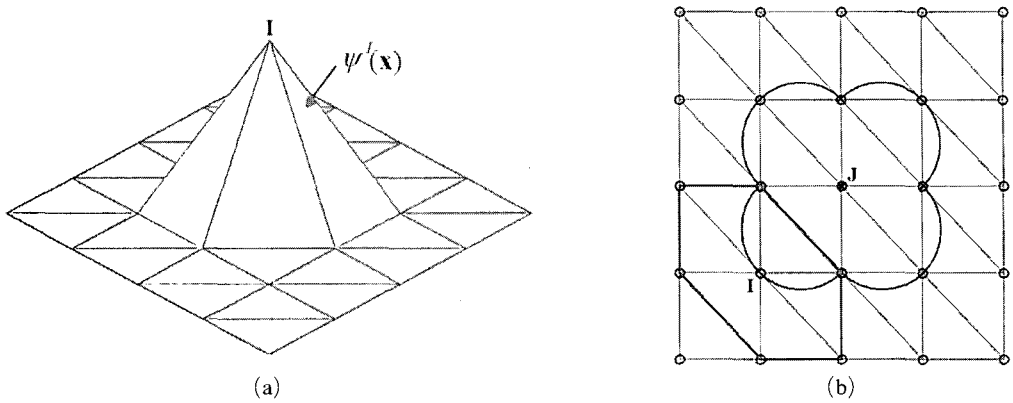

(a) (b)

Fig. 5 In the PG-NE method : (a) CS-FE basis function ; (b) intersection region Ω_{int}^{IJ} between test and trial basis functions

Here, three points $\boldsymbol{x}_1$, $\boldsymbol{x}_2$ and $\boldsymbol{x}_3$ are three vertices of triangle (in the counter-clockwise direction) and the triangle area A is calculated according to

$$A=\{(x_1y_3)(y_2-y_3)-(x_2-x_3)(y_1-y_3)\}/2 \quad (28)$$

4.2 Imposition of essential boundary conditions

As illustrated in Fig. 3, Laplace interpolation functions (e.g. $\phi_J(\boldsymbol{x})$) of the nodes close to the boundary vanish along the boundary. In order to explain this property, let us consider a point $\boldsymbol{x}_P$ located on the boundary $supp(\phi_J)\cap\Gamma$. Then, referring to Fig. 6(a), this point leads to an unbounded Voronoi polygon ω_P with two sides of infinite lengths s_L and s_M. As a result, the denominator of Eq. (5) becomes infinity while $\alpha_J(\boldsymbol{x}_P)$ being kept a finite value, so that we have

$$\lim_{s_L,s_M\to\infty}\phi_J(\boldsymbol{x}_P)=0, \text{ on } \Gamma\cap supp(\phi_J) \quad (29)$$

On the other hand, Laplace interpolation functions (e.g. $\phi_K(\boldsymbol{x})$) of the nodes on the boundary vary from unity at their own nodes to zero at their neighbor nodes along the boundary. Referring to the unbounded Voronoi polygon ω_P of $\boldsymbol{x}_P$ shown in Fig. 6(b), one can realize that α_L and α_M become to be negligible because s_K and s_N are of infinite lengths. Consequently, Eq. (5) becomes

$$\phi_K(\boldsymbol{x}_P)\cong(s_K/h_K)/(s_K/h_K+s_N/h_N) \quad (30)$$

Taking the limit process, we have

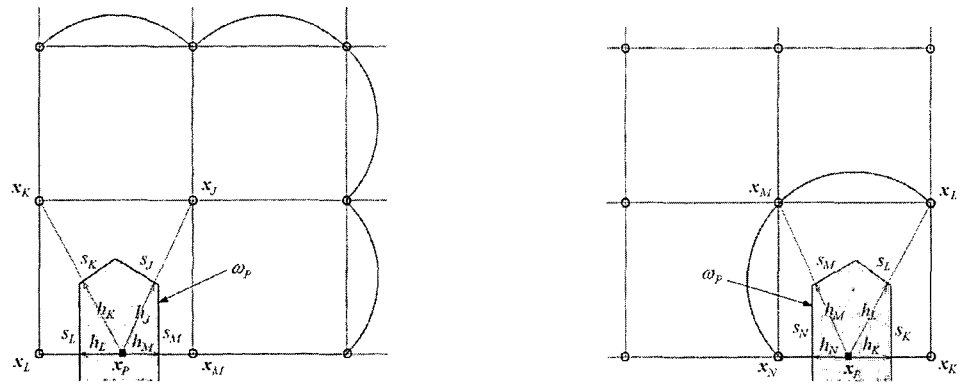

(a) (b)

Fig. 6 Unbounded Voronoi polygons ω_P : (a) for the nodes close to the boundary ; (b) for the nodes on the boundary

$$\lim_{s_K, s_N \to \infty} \phi_K(\boldsymbol{x}_P) = 1 - \frac{d(\boldsymbol{x}_K, \boldsymbol{x}_P)}{d(\boldsymbol{x}_K, \boldsymbol{x}_N)}, \text{ on } \Gamma \cap supp(\phi_K) \quad (31)$$

This clearly shows the linear variation of ϕ_K along the boundary $supp(\phi_K) \cap \Gamma$.

The above two features (29) and (31) do also hold for Laplace interpolation functions in non-convex domain. Let us consider a node I shown in Fig 7, where the region of Delaunay circumcircles that is outside of the boundary is not included in the support of ϕ_I by virtue of the definition (6). Thus, the Laplace interpolation function is not defined in the region outside the boundary, and it possesses a linear variation along the non-convex boundary according to the same argument explained above for the convex domain. The explanation for Laplace interpolation functions of the internal nodes close to the non-convex boundary, that is for the feature (29), is also the same as for the case in convex domain. Thanks to these interpolation features of Laplace functions, one can easily enforce the essential boundary conditions by simply assigning the specified values $\hat{u}_a$ to the corresponding boundary nodes. In other words, the imposition of essential boundary conditions in the natural element method can be accomplished in the same manner as in conventional finite element method.

However, this simple imposition may be broken down for the nodes on the non-convex boundary because the linear consistency along the boundary does not hold any longer (Cueto et al., 2002). In order to illustrate this situation, let us consider a non-convex boundary shown in Fig. 8. Where, the line segment Γ_{I-J} is prescribed to have zero displacement while the remaining part is assumed to be free boundary. Here, we restrict four neighbor nodes of node I, two boundary nodes and two internal nodes, for explanation purpose, then we have three Delaunay triangles and Delaunay circumcircles. Within this restricted grid, Laplace interpolation function ϕ_I has the support given by

$$supp(\phi_I) = (cir(\Delta_{IJK}) \cup cir(\Delta_{IKM}) \cup (\Delta_{IML})) \cap \Omega^{CH}(\aleph) \quad (32)$$

The supports of other four Laplace interpolation functions can be easily realized from the definition (6). Since two functions ϕ_K and ϕ_M vanish on the boundary by virtue of the feature (29), those do not cause any trouble even in non-convex boundary. But, since Laplace interpolation function ϕ_L does not vanish along the line segment Γ_{I-J}, the displacement interpolation along this segment is expressed by

$$u_a(\boldsymbol{x}) = u_a^I \phi_I(\boldsymbol{x}) + u_a^J \phi_J(\boldsymbol{x}) + u_a^L \phi_L(\boldsymbol{x}), \text{ on } \Gamma_{I-J} \quad (33)$$

Thus, the prescribed essential boundary condition can be satisfied only when the nodal values u_a^L are enforced to be zero. But, this enforcement is not possible because the free boundary condition is prescribed on the line segment Γ_{L-I}.

This difficulty in dealing with the essential boundary condition specified on the non-convex boundary can be resolved by employing the algorithm proposed by Sambridge et al.(1995). According to this algorithm, any two Delaunay circumcircles can not be overlapped when their Delaunay triangles do not share a common edge. Now, let us examine three Delaunay circumcircles

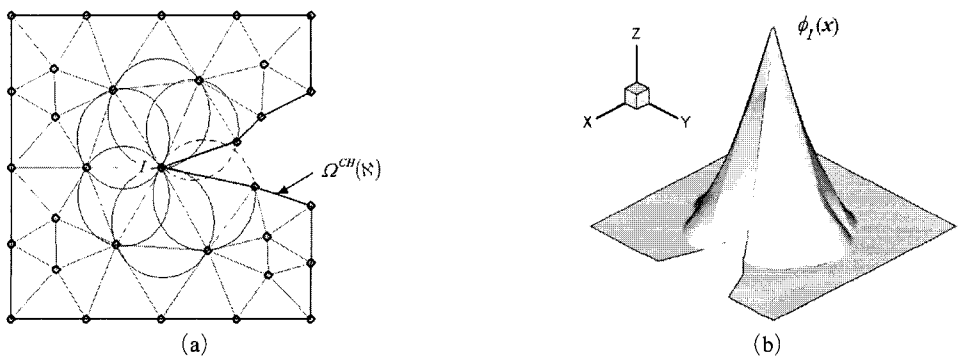

Fig. 7 Laplace interpolation function in non-convex domain

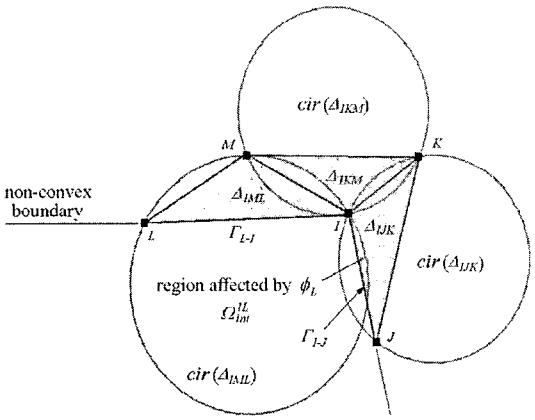

Fig. 8 Disobedience of the linear consistency along the non-convex boundary

shown in Fig. 8. We can find out that the Delaunay circumcircle $cir(\Delta_{IJK})$ can be overlapped with the Delaunay circumcircle $cir(\Delta_{IKM})$ but it can not be overlapped with the Delaunay circumcircle $cir(\Delta_{IML})$. Thus, the overlapping between $cir(\Delta_{IJK})$ and $cir(\Delta_{IML})$ can not be defined, so that the region denoted by Ω_{int}^{IL} can not be the support of the Laplace interpolation function $\phi_L(x)$. Then, the Sambridge algorithm allows us to have

$$u_\alpha(\boldsymbol{x}) = u_\alpha^I \phi_I(\boldsymbol{x}) + u_\alpha^J \phi_J(\boldsymbol{x}), \text{ on } \Gamma_{I-J} \quad (34)$$

As a result, one can impose the essential boundary condition specified on the non-convex boundary as easily as in the convex boundary.

5. Numerical Experiments

A test Fortran program was coded according to the numerical formulations described in previous sections, and it was interfaced with pre- and post-processing modules of ANSYS commercial code (Ansys, Inc., 1998) for grid generation and graphic visualization. Restricting to the two-dimensional linear elasticity, we perform both the patch test and the convergence assessment. For the convergence evaluation, we use the relative energy-norm error defined by

$$\frac{\|\boldsymbol{u}-\boldsymbol{u}^h\|_{E(\Omega)}}{\|\boldsymbol{u}\|_{E(\Omega)}} = \frac{\left\{\int_\Omega ((\varepsilon_{\alpha\beta}(\boldsymbol{u})-\varepsilon_{\alpha\beta}(\boldsymbol{u}^h))(\sigma_{\alpha\beta}(\boldsymbol{u})-\sigma_{\alpha\beta}(\boldsymbol{u}^h)))\, d\Omega\right\}^{1/2}}{\left\{\int_\Omega (\varepsilon_{\alpha\beta}(\boldsymbol{u})\sigma_{\alpha\beta}(\boldsymbol{u}))\, d\Omega\right\}^{1/2}} \quad (35)$$

with the exact solution denoted by $\boldsymbol{u}$. To each Delaunay triangle in the background cell, we use 3 Gauss points for the numerical integration and 13 Gauss points for the post-processing of strains, stresses and energy-norm errors. In order to obtain smoother and continuous strain and stress fields, we perform the stress recovery of the nodal stresses by the stress projection method (Zienkiewicz and Taylor, 1989), because strain and stress fields approximated display jumps at individual nodes, as presented in the numerical results by Sukumar et al.(1998). Material properties for all the model problems considered here are commonly taken as follows: $E=2.0\times10^{11}Pa$ and $\upsilon=0.3$.

5.1 Patch test

We consider two simulation cases shown in Figs. 9(a) and 9(b) for the patch test of the PG-NE method, where both problems are in plane stress condition. Through the displacement patch test with $u_x=u_y=1\times10^{-3}$ m, we intend to examine the attainment of uniform strain and stress fields. On the other hand, we check the uniaxial plane stress field in the equilibrium patch test for which uniform normal traction $\hat{t}_x=1.0Pa$ is applied to the right side. Figure 10 represents uniform and non-uniform grid patterns prepared for both patch tests. We simulate two patch test problems by PG-NE and BG-NE methods, with both grids, and we compare the numerical results.

The PG-NE method provides the relative energy-norm errors close the machine precision of $O(10^{-16})$ in four simulation cases, as recorded in Table 1, so that it passes the patch test. On the other hand, we see that the BG-NE method does not pass the patch test with the considerably high level of relative energy-norm errors. Reminding the linear consistency property (10) of Laplace interpolation functions, we can confirm that the patch test failure in the BG-NE method is owing to the numerical integration error. While, this critical integration error is completely eliminated in the PG-NE method according to the use of Delaunay-triangle-based test functions. In papers by Sukumar et al.(1998) and Cueto et al.(2002),

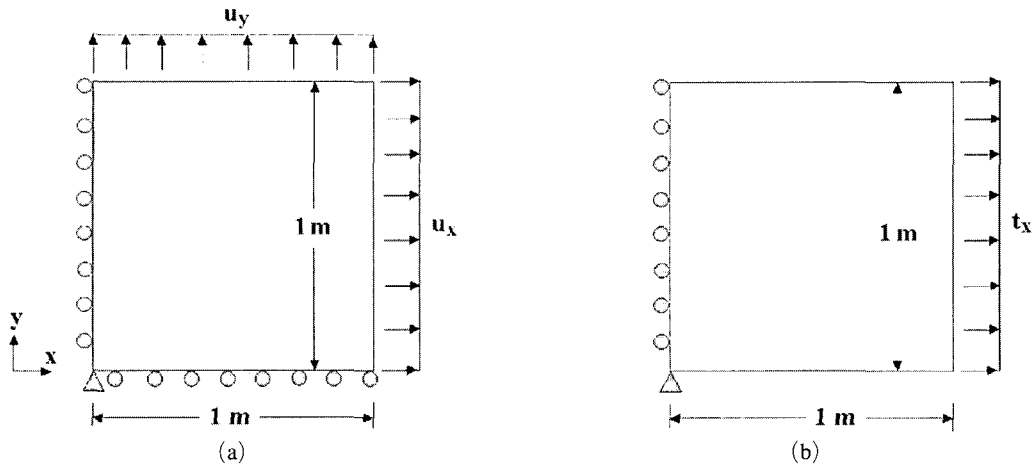

Fig. 9 Models for the patch test: (a) displacement patch test; (b) equilibrium patch tes

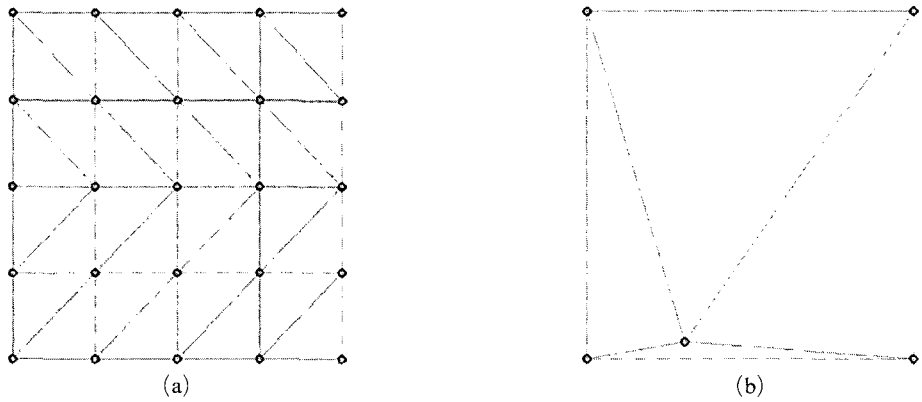

Fig. 10 Grid patterns for the patch test: (a) uniform; (b) non-uniform

Table 1 Relative energy-norm errors $\|\boldsymbol{u}-\boldsymbol{u}^h\|_{E(\Omega)}/\|\boldsymbol{u}\|_{E(\Omega)}$ in the patch test

Test type	Grid	BG-NE method	PG-NE method
Displacement	Uniform	$3.72E-02$	$1.32E-15$
	Non-uniform	$6.53E-02$	$9.14E-16$
Equilibrium	Uniform	$4.76E-02$	$1.08E-14$
	Non-uniform	$4.15E-02$	$1.42E-15$

the assessment of numerical integration accuracy of the BG-NE method using Sibsonian interpolation functions is addressed in details.

For the displacement patch test with the uniform grid, we compare distributions of the effective stress between the BG-NE and the PG-NE method in Fig. 11. Contrary to the PG-NE method, the BG-NE method leads to the non-uniformity in the stress field, particularly at four edges. This non-uniform stress field by the BG-NE method was commonly observed in the remaining three patch test cases. In general, the numerical error and the resulting non-uniformity in stress field owing to the inconsistency of the integrand support with the regular integration region do commonly occur in other meshfree methods. For an example, the EFGM using higher Gauss-Legendre quadrature rule with rectangular background cell leads to the relative L^2-norm error in the range of $O(10^{-6})$ (Dolbow and

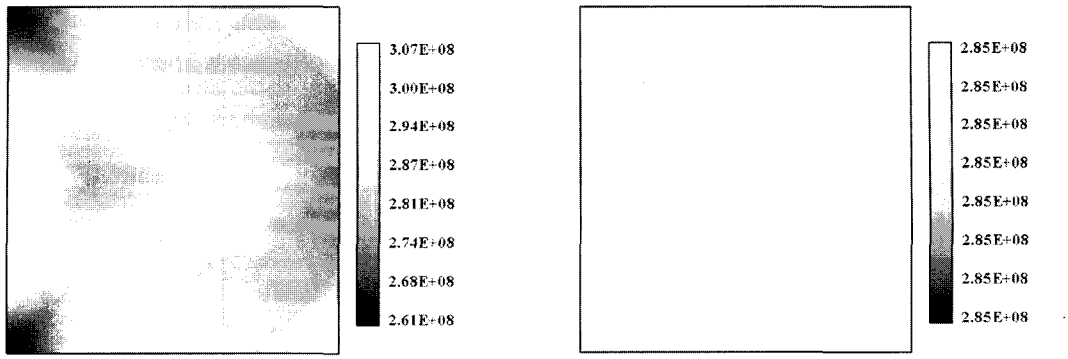

Fig. 11 Distributions of the effective stress in the displacement patch test with the uniform grid : (a) BG-NE method ; (b) PG-NE method

Belytschko, 1999).

5.2 Experiment for the convergence assessment

We next consider an infinite plate with a circular hole, which is subject to unidirectional tension in the x-direction under plane strain condition. Its numerical analysis model with finite dimensions $2L\times 2L$ is depicted in Fig. 12, together with geometric dimensions and traction boundary condition. Referring to a book by Timoshenko and Goodier (1970), we have exact solutions of the problem with t_x of $1.0Pa$:

$$u_x(r,\theta)=\frac{a}{8\mu}\left[\frac{r}{a}(\kappa+1)\cos\theta+\frac{2a}{r}\{(\kappa+1)\cos\theta+\cos 3\theta\}-\frac{2a^2}{r^3}\cos 3\theta\right] \tag{36}$$

$$u_y(r,\theta)=\frac{a}{8\mu}\left[\frac{r}{a}(\kappa-3)\sin\theta+\frac{2a}{r}\{(-\kappa+1)\sin\theta+\sin 3\theta\}-\frac{2a^2}{r^3}\sin 3\theta\right] \tag{37}$$

$$\sigma_{xx}(r,\theta)=1-\frac{a^2}{r^2}\left(\frac{3}{2}\cos 2\theta+\cos 4\theta\right)+\frac{3a^4}{2r^4}\cos 4\theta \tag{38}$$

$$\sigma_{yy}(r,\theta)=-\frac{a^2}{r^2}\left(\frac{1}{2}\cos 2\theta-\cos 4\theta\right)-\frac{3a^4}{2r^4}\cos 4\theta \tag{39}$$

$$\sigma_{xy}(r,\theta)=-\frac{a^2}{r^2}\left(\frac{1}{2}\sin 2\theta+\sin 4\theta\right)+\frac{3a^4}{2r^4}\sin 4\theta \tag{40}$$

where μ is the shear modulus. And, κ is the Kolosov constant defined by $\kappa=(3-\nu)/(1+\nu)$ in plane strain condition and $\kappa=(3-\nu)$ in plane stress condition. Fig. 13 represents two grid patterns used for the convergence analysis, where the locally refined grid was generated from the almost uniform grid shown in Fig. 13(a) by adding more nodes in the vicinity of circular hole.

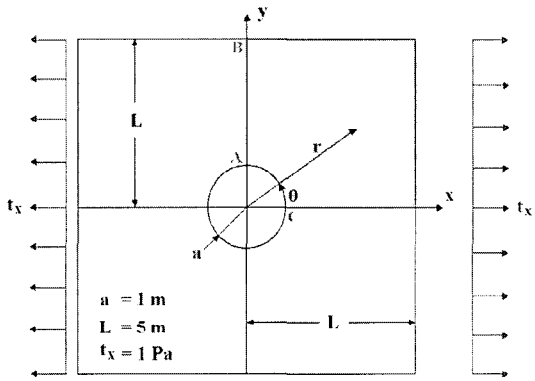

Fig. 12 Plate with a circular hole under unidirectional tension

Convergence rates of the relative energy-norm error in the BG-NE and the PG-NE methods are represented in Fig. 14(a) for the uniform grid and Fig. 14(b) for the locally refined one, respectively. The PG-NE method shows smaller energy-norm errors in the absolute magnitude and more steep convergence rates than the BG-NE method for both grid patterns. Meanwhile, the convergence rates in the BG-NE method deteriorate with the grid density increase, contrary to the PG-NE method possessing uniform convergence rates. In connection with the previous patch test,

the affection of numerical integration error in the BG-NE method is also manifest from the convergence assessment. On the other hand, the numerical integration accuracy in the PG-NE method

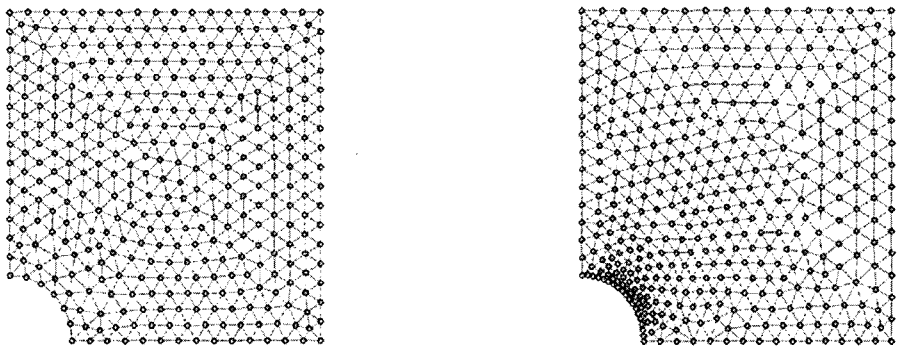

(a) (b)

Fig. 13 Grids: (a) uniform (368 nodes); (b) locally refined (410 nodes)

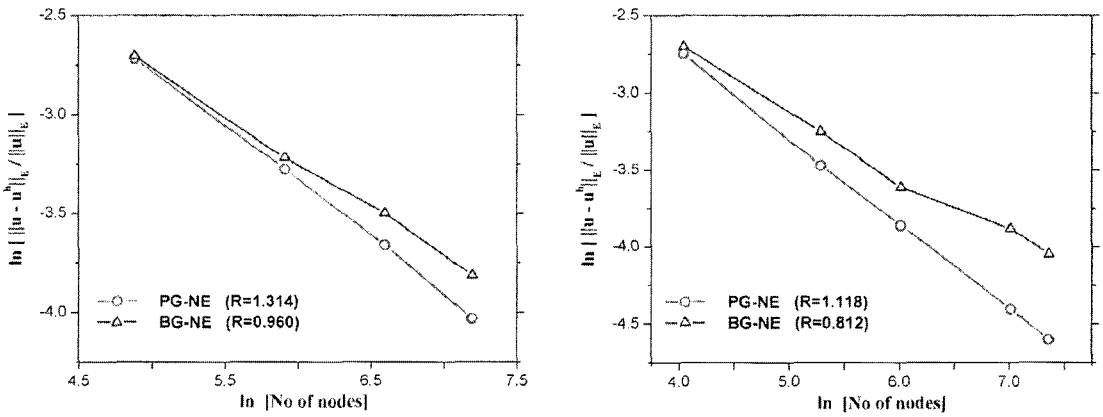

(a) (b)

Fig. 14 Convergence rates in the energy-norm sense: (a) uniform grid; (b) locally refined grid

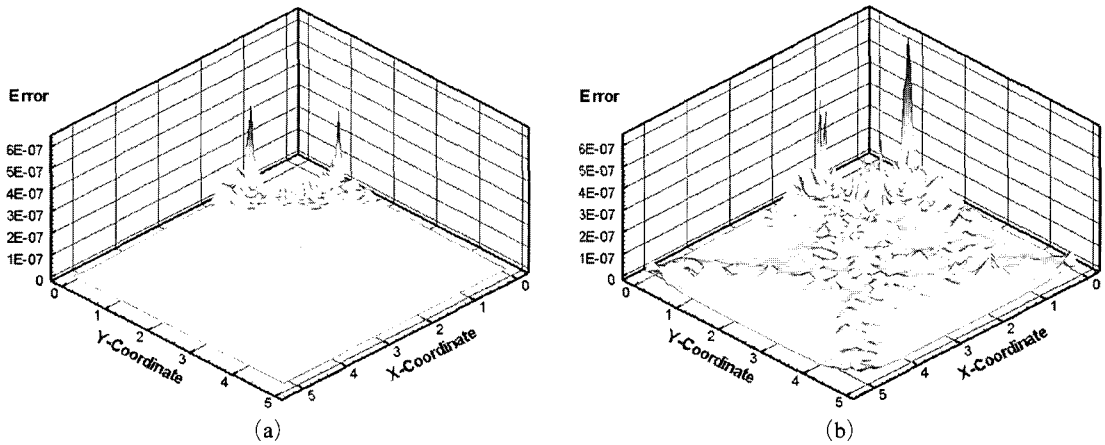

(a) (b)

Fig. 15 Distributions of local energy-norm errors (locally refined grid with 1,569 nodes): (a) PG-NE method; (b) BG-NE method

has been justified once more.

Figures 15(a) and 15(b) show distributions of the local energy-norm errors $\| \boldsymbol{u}-\boldsymbol{u}^h \|_{E(x)}$ defined by

$$\| \boldsymbol{u}-\boldsymbol{u}^h \|_{E(x)} = \left\{ \frac{1}{2} (\varepsilon_{\alpha\beta}(\boldsymbol{u}) - \varepsilon_{\alpha\beta}(u^h)) (\sigma_{\alpha\beta}(\boldsymbol{u}) - \sigma_{\alpha\beta}(u^h)) \right\}^{1/2} \quad (41)$$

in the PG-NE and the BG-NE methods, respectively. In Eq. (41), $\boldsymbol{x}$ denote 13 Gauss points within individual Delaunay triangles. In the PG-NE method, relatively high local errors are concentrated around the circular hole edge, and which is a typical pattern observed commonly in standard finite element method owing to the stress concentration in the vicinity of circular hole. On the other hand, the BG-NE method produces a widespread error distribution, particularly along two diagonals of the plate as well as the circular hole edge. Thus, one can clearly see that the numerical integration error occurs over entire problem domain, regardless of the stress concentration.

Figure 16(a) compares the distributions of normal stress σ_{xx} with the exact solution, along the line A-B in Fig. 12. Where, both the BG-NE and PG-NE solutions were obtained with a locally refined grid composed of 1,569 nodes. The

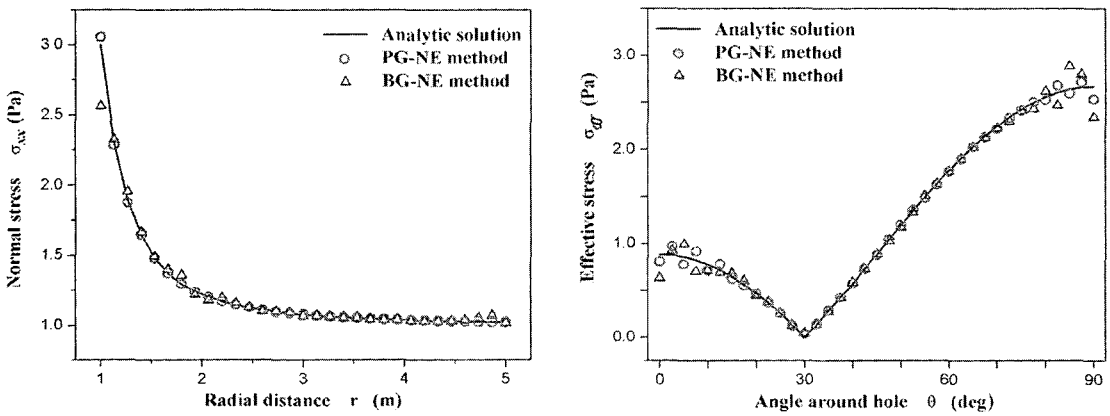

(a) (b)

Fig. 16 Comparison of stress distributions with exaction solutions : (a) normal stress σ_{xx} along the vertical line A-B ; (b) effective stress along the circular path C-A

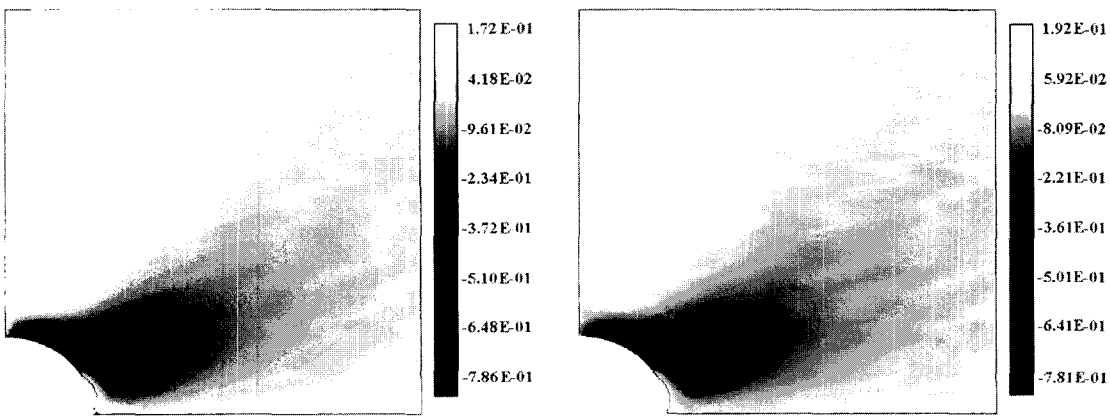

(a) (b)

Fig. 17 Contours of the shear stress σ_{xy} (locally refined grid composed of 1,569 nodes) : (a) PG-NE method ; (b) BG-NE method

normal stress distribution obtained by the PG-NE method is shown to be in excellent agreement with the exact one. But, the BG-NE method not only shows a remarkable discrepancy in the peak stress value but also noticeable oscillations in the distribution. Referring to Fig. 16(b) representing the comparison of the effective stress distributions with the exact solution, along the circular path C-A, both the BG-NE and the PG-NE display the considerable oscillations near $\theta=0$ and $\pi/2$. As is well addressed in a paper by Cho and Oden (1997), finite element solutions commonly display the oscillation behavior, while being suppressed by using locally refined meshes to a certain extent, in stress distributions where the boundary layer singularity exists. However, the BG-NE method produces more significant oscillations than the PG-NE method, and which can be explained by the numerical integration error because the same grid was used for both methods.

The oscillation phenomenon caused by the numerical integration error in the BG-NE method can be clearly observed from the comparison of shear stress distributions shown in Fig. 17 between the BG-NE and the PG-NE methods. The oscillation pattern in the stress contour by the BG-NE method is shown to be closely consistent with the local error distribution shown in Fig. 15(b). As is worse, the BG-NE method leads to the peak shear stress value $0.192Pa$ which remarkably deviates from the exact solution 0.176 Pa, when compared to $0.172Pa$ obtained by the PG-NE method.

6. Conclusion

A natural element method based upon the Petrov-Galerkin approximation concept, so called the PG-NE method, has been introduced, in order to secure the numerical integration accuracy. To define a test basis function we used the Delaunay-triangle-supported constant strain finite elements, while employing Laplace interpolation functions based on the natural neighbors for trial basis functions. A combination of the Delaunay-triangle-supported background cells and test basis functions exactly coincides the integrand function supports with the regular Gauss integration regions, so that the inherent numerical integration errors occurred in most mesh free methods has been successfully eliminated. As well as, the imposition of essential boundary conditions has been directly and strictly accomplished according to the basic properties of Laplace interpolation functions, even for non-convex boundaries.

From the 2-D linear elasticity benchmark tests, we confirmed that the PG-NE method does not suffer from the numerical integration inaccuracy at all such that it provides the very accurate energy-norm error close the machine precision. While, the BG-NE method has shown to be significantly influenced by the numerical integration error. In the convergence assessment experiment, the PG-NE method provides higher and uniform convergence rates, when compared to the BG-NE method showing the convergence deterioration non-uniformly with the grid density increase owing to the existence of numerical integration error. The comparison of distributions of stresses and local energy-norm errors has clearly justified the numerical integration accuracy of the PG-NE method. Contrary to the BG-NE method causing the widespread fluctuations in those distributions, the PG-NE method shows the fluctuation stemming from only the boundary layer that is restricted in the vicinity of the circular hole edge.

The non-symmetry of stiffness matrix, a drawback of the PG-NE method, is an indispensable penalty to pay for achieving both the numerical integration accuracy and the direct imposition of essential boundary condition. Furthermore, it is a less critical issue nowadays thanks to the advances in both computation facilities and technologies like parallel computing.

Acknowledgments

The authors gratefully acknowledge the financial support for this work by Korea Industrial Technology Foundation (June 2003-April 2006).

References

ANSYS, Inc., 1998, User's Manual (ver. 5.5.1), Houston, PA.

Atluri, S. N. and Zhu, T., 1998, "A New Meshless Local Petrov-Galerkin (MLPG) Approach in Computational Mechanics," *Computational Mechanics*, Vol. 22, pp. 117~127.

Belikov, V. V., Ivanov, V. D., Kontorovich, V. K., Korytnik, S. A. and Semenov, A. Yu, 1997, "The Non-Sibsonian Interpolation: a New Method of Interpolation of the Values of a Function on an Arbitrary Set of Points," *Comput. Math. Math. Phys.*, Vol. 37, pp. 9~15.

Belytschko, T., Lu, Y. Y. and Gu, L., 1994, "Element-free Galerkin Methods," *Int. J. Numer. Methods Engng.*, Vol. 37, pp. 229~256.

Braun, J. and Sambridge, M., 1995, "A Numerical Method for Solving Partial Differential Equations on Highly Irregular Evolving Grids," Nature, Vol. 376, pp. 655~660.

Cho, J. R. and Lee, S. Y., 2002, "Dynamic Analysis of Baffled Fuel-Storage Tanks Using the ALE Finite Element Method," *Int. J. Numer. Methods Fluids*, Vol. 41, pp. 185~208.

Cho, J. R. and Oden, J. T., 1997, "Locking and Boundary Layer in Hierarchical Models for Thin Elastic Structures," *Comput. Methods Appl. Mech. Engrg.*, Vol. 149, pp. 33~48.

Cueto, E., Calvo, B. and Doblare, M., 2002, "Modelling Three-Dimensional Piece-wise Homogeneous Domains Using the Shape-based Natural Element Method," *Int. J. Numer. Methods Engng.*, Vol. 54, pp. 871~897.

Dolbow, J. and Belytschko, T., 1999, "Numerical Integration of the Galerkin Weak Form in Meshfree Methods," *Computational Mechanics*, Vol. 23, pp. 219~230.

Duarte, C. A. and Oden, J. T., 1996, "An h-p Adaptive Method Using Clouds," *Comput. Methods Appl. Mech. Engrg.*, Vol. 139, pp. 237~262.

Farin, G., 1990, "Surface over Dirichlet Tessellations," *Comput. Aided Geom. Des.*, Vol. 7, No. 1-4, pp. 281~292.

Green, P. J. and Sibson, R., 1978, "Computing Dirichlet Tessellations in the Plane," *The Computer Journal*, Vol. 21, pp. 168~173.

Hiyoshi, H. and Sugihara, K., 1999, "Two Generalization of an Interpolant based on Voronoi Diagrams," *Int. J. Shape Modeling*, Vol. 5, pp. 219~231.

Liu, W. K., Jun, S. and Zhang, Y. F., 1995, "Reproducing Kernel Particle Methods," *Int. J. Numer. Methods Fluids*, Vol. 20, pp. 1081~1106.

Melenk, J. M. and Babuska, I., 1996, "The Partition of Unity Finite Element Method: Basic Theory and Applications," *Comput. Methods Appl. Mech. Engrg.*, Vol. 139, pp. 289~314.

Nayroles, B., 1992, "Generalizing the Finite Element Method: Diffuse Approximation and Diffuse Elements," *Computational Mechanics*, Vol. 10, pp. 307~318.

Okabe, A., Boots, B. and Sugihara, K., 1992, *Spatial Tessellations : Concepts and Applications of Voronoi Diagrams*, John Wiley & Sons, England.

Piper, P., 1993, "Properties of Local Coordinates based on Dirichlet Tessellations," *in Farin, G., Hagan, H. and Noltemeier, H. (eds.), Geometric Modelling*, Vol. 8, pp. 227~239.

Sambridge, M, Braun, J. and McQueen, H, 1995, "Geophysical Parameterization and Interpolant of Irregular Data Using Natural Neighbors," *Geophysical Journal International*, Vol. 122, pp. 837~857.

Sibson, R., 1980, "A Vector Identity for Dirichlet Tessellation," *Mathematical Proc. the Cambridge Philosophical Society*, Vol. 80, pp. 151~155.

Strang, G. and Fix, G. J., 1973, *An Analysis of the Finite Element Method*, Prentice-Hall, New Jersey.

Sukumar, N, and Moran, A. and Belytschko, T., 1998, "The Natural Element Method in Solid Mechanics," *Int. J. Numer. Methods Engng.*, Vol. 43, pp. 839~887.

Timoshenko, S. P. and Goodier, J. N., 1970, *Theory of Elasticity*, McGraw-Hill, New York.

Traversoni, L., 1994, "Natural Neighbor Finite Elements," *Proc. Int. Conf. Hydraulic Engineering Software*, Vol. 2, pp. 291~297.

Zhu, T. and Atluri, S. N., 1998, "A Modified

Collocation Method and a Penalty Formulation for Enforcing the Essential Boundary Conditions in the Element Free Galerkin Method," *Computational Mechanics*, Vol. 21, pp. 211~222.

Zienkiewicz, O. C. and Taylor, R. L., 1989, *The Finite Element Method : Basic Formulation and Linear Problems*, McGraw-Hill, Singapore.